MATERIAL LIMITS OF SILICON FROM STATE-OF-THE-ART PHOTOLUMINESCENCE IMAGING TECHNIQUES

Florian Schindler[a,b], Johannes Giesecke[a], Bernhard Michl[a], Jonas Schön[a], Patricia Krenckel[a], Stephan Riepe[a], Wilhelm Warta[a], Martin C. Schubert[a]

[a] Fraunhofer Institute for Solar Energy Systems (ISE), Heidenhofstr. 2, D-79110 Freiburg, Germany
[b] Freiburg Materials Research Center (FMF), Albert-Ludwigs-Universität Freiburg, Stefan-Meier-Str. 21, D-79104 Freiburg, Germany
Ph +49 761 4588 5321, Fax +49 761 4588 9250, Email: florian.schindler@ise.fraunhofer.de

ABSTRACT: This work reports on state-of-the-art silicon material characterization by calibrated photoluminescence imaging (PLI). PL imaging techniques allow for a characterization of a large variety of material properties, ranging from bulk and surface recombination properties of bare silicon ingots, to crystal structure, dopant concentration and bulk lifetime of silicon wafers up to material limiting impurities. In combination with solar cell simulations, injection-dependent PLI of processed wafers provides a method for determining the material's efficiency potential. In this contribution, we present two methods for imaging the concentration of interstitial iron at passivated silicon slices and at unpassivated silicon ingots. The latter is achieved by our latest progress in PL-based charge carrier bulk lifetime measurements with highest sensitivity, giving access to the bulk recombination properties of the ingot. Additionally, we present an improved analysis of specific loss mechanisms in silicon based on de-smeared injection-dependent lifetime images of processed wafers, which is demonstrated on the example of the bulk-related efficiency limitations in high-performance multicrystalline silicon. This latest progress rounds off the established techniques, enhancing the potential of PL based imaging techniques for a comprehensive assessment of silicon material quality, from limitations in bare silicon ingots to efficiency loss mechanisms in processed samples.

Keywords: Photoluminescence imaging, iron imaging, modulated PL, efficiency limits, multicrystalline silicon

1 INTRODUCTION

Photoluminescence-based characterization techniques have been successfully established in silicon material characterization labs during the past decade, both in research and industry. Its remarkably high sensitivity and non-destructive character together with its simplicity gave rise to the development of a large variety of applications, ranging from measurements of material parameters like crystal defects, doping concentration, charge carrier lifetime and concentration of specific impurities to also solar cell properties like local current and voltage, series resistance and interface recombination. An overview of the majority of these measurement techniques is given in [1].

In this contribution, we demonstrate how to identify material limits of silicon by state-of-the-art photoluminescence imaging techniques. We include our latest advances and innovations which enable a deeper insight into the material limitations directly after crystallization by iron imaging at vertical silicon slices and bare silicon ingots. The exact identification and quantification of bulk-related efficiency losses after selected solar cell processing steps is extended to separating between recombination- and diffusion-related losses.

2 DEVELOPMENT OF PL-BASED MEASUREMENT TECHNIQUES

Improvement of silicon solar cell efficiencies requires a fundamental knowledge of material limitations, many of which can be assessed by already established photoluminescence-based measurement techniques. Measurements at bare silicon ingots allow for a determination of bulk lifetime and surface recombination velocity [2], as well as for a quantification of interstitial iron concentrations [3]. Further, PL imaging of unpassivated silicon wafers allows for determination of the most recombination active wafer regions, such as dislocation clusters and edge regions in multicrystalline silicon, and, thus, enables a first quality rating of the material [4]. Apart from areas of strongly recombination active crystal defects, the charge carrier density in as-cut wafers is limited by recombination at the unpassivated surfaces. Given a sufficiently high and uniform surface recombination velocity, the PL signal is determined by the majority charge carrier concentration. Under low-level injection, this enables a spatially resolved determination of the doping concentration [5]. PL imaging at surface-passivated wafers [6] combined with different calibration techniques [7, 8] gives access to spatially resolved bulk recombination properties and, in combination with metastable defect imaging [9], allows for measuring the concentrations of interstitial iron [10] and chromium [11] in p-type silicon with a detection limit in the range of 10^{10} cm^{-3} as well as a relative concentration of the boron-oxygen defect [9, 12]. Another approach is based on the growth of thermal donors and provides images of the interstitial oxygen concentration [13]. As these methods exploit the different recombination activity of metastable defects (Fe$_i$/FeB, Cr$_i$/CrB, BO$_{degraded}$/BO$_{annealed}$) or the impact of defect redistribution on resistivity (creation of thermal donors for O$_i$-imaging), they are not suited for the identification of initially unknown impurities. Access to such defects can be obtained by making use of the temperature and injection dependence of charge carrier lifetime. In combina-

tion with PL imaging, this approach enables a spatially resolved identification of further material limiting impurities [14].

In order to deepen the understanding of silicon material limits, our recent research in PL-based characterization techniques focused on measuring the distribution and concentration of interstitial iron across silicon ingots after crystallization. The first approach presented in section III.A is based on lifetime measurements at passivated vertical silicon slices. The development of a method for iron imaging at unpassivated silicon ingots, making use of highly-sensitive charge carrier bulk lifetime measurements at unpassivated ingots [2, 15], is discussed in section III.B. This renders unnecessary the preparation of vertical slices. Finally, the innovations in efficiency-limiting bulk recombination analyses (ELBA) [16, 17] in combination with a de-smearing of PL images for quantification of specific loss mechanisms in the material are sketched in section III.C. We are now able to separate local recombination from diffusion effects quantitatively. Thus, we prove that grain boundaries account for the major part of efficiency losses in high-performance multicrystalline silicon, comprising losses due to recombination of charge carriers at the grain boundaries and due to diffusion of charge carriers from grains to grain boundaries, where they can subsequently recombine. This knowledge could be of importance for a further optimization of crystallization parameters for the production of high performance multicrystalline silicon in order to reduce material-related efficiency losses.

3   RESULTS

3.1 Iron imaging at silicon slices

Iron imaging at passivated silicon wafers is a well-established method for spatially resolved determination of interstitial iron concentration in silicon bulk material [9, 10, 18]. This method is well suited for tracking the interstitial iron concentration in wafers along the solar cell processing chain, as measurements can be performed at passivated lifetime samples at any stage of processing. Thus, the impact of high-temperature steps on the concentration of interstitial iron can be assessed. However, if the interstitial iron distribution along the ingot height shall be determined, horizontal wafers of several ingot positions or a vertical wafer are required. Alternatively, a thick vertical silicon slice can be cut off from the side of the ingot before wafering. Thus, a vertical silicon sample is obtained, while horizontal wafering of the ingot is still possible. The procedure for iron imaging at passivated silicon wafers can be transferred to passivated vertical slices. However, the larger thickness of vertical slices (~ 2 mm) implies some modifications, which are outlined in the following.

We compare a p-type 1 Ωcm surface-passivated silicon wafer with a thickness of $d = 200$ μm and a constant injection-independent bulk lifetime of $\tau = 100$ μs with a 2 mm thick surface-passivated silicon slice featuring

the same doping and bulk lifetime. The front- and back-surface recombination velocities are assumed to be $S_f = S_b = 1$ cms^{-1} for both samples, and a typical reflection of $R(790\,\text{nm}) = 0.27$ for aluminum oxide passivated samples was used in the calculations. The steady-state excess charge carrier density profile $\Delta n(z)$ in z-direction along the sample depth (perpendicular to the surfaces) can be calculated by solving the steady-state continuity equation

$$-D_e \frac{\partial^2 \Delta n(z)}{\partial z^2} + \frac{\Delta n(z)}{\tau} = G(z) \qquad (1)$$

with D_e the diffusion coefficient for electrons and $G(z)$ the monoexponential generation rate for an irradiation of 1 sun with a 790 nm laser at the front surface of the samples in combination with the following boundary conditions:

$$D_e \frac{\partial \Delta n}{\partial z}\bigg|_{z=0} = S_f \Delta n(z = 0) \qquad (2a)$$

$$D_e \frac{\partial \Delta n}{\partial z}\bigg|_{z=d} = -S_b \Delta n(z = d) \qquad (2b)$$

Further details on the solution of these equations can be found in [19]. Figure 1 shows the $\Delta n(z)$-profiles for both samples.
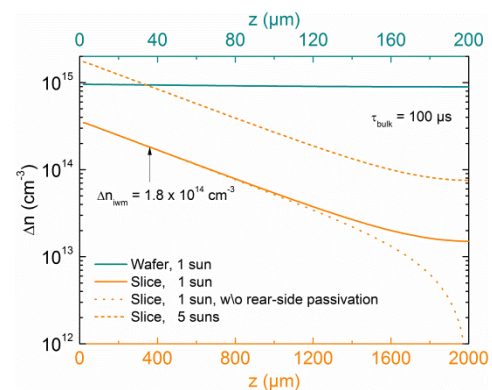

Figure 1: Comparison of excess charge carrier profile across the thickness of a surface-passivated silicon wafer with a thickness of 200 μm and a silicon slice with a thickness of 2 mm featuring double- or single-side surface-passivation (constant bulk lifetime 100 μs, illumination 1 sun or 5 suns with a 790 nm laser, $R = 0.27$).

While excess charge carriers distribute virtually homogeneously across the sample thickness of passivated silicon wafers (solid cyan curve), the charge carrier density decreases exponentially towards the backside of the silicon slice (solid orange curve), which is attributed to the thickness (2 mm) being significantly larger than the minority charge carrier diffusion length (~ 519 μm) and the exponentially decreasing generation rate. Thus, for passivated silicon wafers, the excess charge carrier density does not have to be regarded as a function of depth, which considerably simplifies the evaluations according to the following relation between the local PL-signal ϕ_i, measured by PL-imaging at pixel i, the local excess charge carrier density Δn_i and net doping concentration n_{net}

$$\phi_i = a \cdot \Delta n_i \cdot (\Delta n_i + n_{net}) = a \cdot G \cdot \tau_i \cdot (G \cdot \tau_i + n_{net}) \qquad (3)$$

which can be directly converted into the local charge carrier lifetime τ_i for a known steady-state depth-averaged generation rate G. The calibration factor a is obtained from modulated photoluminescence measurements as described in [8, 19]. In the case of thin wafers with diffusion lengths typically not much less than wafer thickness, it is convenient to use a depth-averaged excess carrier generation rate G with incident photon flux density j_γ and front reflection $R(790 \text{ nm})$ according to:

$$G = (1 - R(790 \text{ nm})) \cdot j_\gamma / w \qquad (4)$$

For our evaluations, we make use of a 1 sun equivalent of

$$j_{\gamma,1\text{sun}}(w = 200 \,\mu\text{m}, T = 300\text{K}) = 2.5 \cdot 10^{17} \text{cm}^{-2}\text{s}^{-1} \qquad (5)$$

Consequently, the calibration of PL-images directly delivers a correct pair of values for $\tau_i(\Delta n_i)$. For thick slices, where the charge carrier density becomes a function of depth, the situation is more complex. For calibrating PL-images of thick slices, we proceed as follows. First, the PL-image is calibrated to lifetime values in the same way as for wafers [8, 19]. For low-level injection conditions, which hold for all of our evaluations, this procedure delivers a correct value for τ_i. However, the obtained injection level Δn_i strongly differs from the correct injection level related to the measured lifetime, as the arithmetic depth average of excess carrier generation rate is only appropriate for uniform excess carrier density depth distributions. For evaluating the interstitial iron concentration, the exact injection level Δn_i relating to the measured τ_i is required. Therefore, the correct averaging across $\Delta n(z)$ has to be applied. As discussed in detail in [20-22], the intensity-weighted mean along the sample depth correctly accounts for the contribution of $\Delta n(z)$ to the measured PL-intensity. Thus, we obtain the correct injection-level Δn_i related to the measured lifetime τ_i by simulating $\Delta n(z)$ according to equations (1) and (2) with the measured lifetime τ_i as input and taking the intensity-weighted mean along the z-direction. Note that this approach assumes an injection-independent charge carrier lifetime for the simulation of $\Delta n(z)$. This is a good approximation, as measurements are performed in low level injection (maximum charge carrier densities are below $5 \cdot 10^{12}$ cm^{-3} for all measurements presented in this work, where even the Fe$_i$-limited lifetime features a weak injection dependence only) and, more importantly, due to the intensity-weighted mean the majority of the signal stems from regions of largest charge carrier density close to the front surface with a small spread in Δn.

In addition to relating a correct $\tau_i(\Delta n_i)$ to each pixel of the PL-image, for vertical slices the net doping concentration changes with position. By applying either spatially resolved four-point-probe or eddy-current measurements, we account for this variation in net doping concentration in the evaluations. All further calculations are identical with the evaluation for interstitial iron imaging at silicon wafers.

As can be seen from Figure 1, at identical illumination conditions the charge carrier density is significantly lower for thick slices than for thin wafers. Thus, care has to be taken to ensure a complete splitting of iron-boron pairs for preparing the Fe$_i$-state, which is obtained by illuminating the samples with an illumination intensity of approximately 5 suns. This delivers an average excess charge carrier density comparable to that obtained on wafer level with an illumination intensity of 1 sun (*cf.* dashed orange curve in Figure 1).

While the strong decay of $\Delta n(z)$ along the depths for thick samples complicates the evaluations, it comes along with an advantage for sample preparation. For a thickness of approximately 2 mm, it renders unnecessary the rear-surface passivation. The charge carrier profile $\Delta n(z)$ for a slice without rear-surface passivation is included in Figure 1 (dotted orange curve). Differences compared with the double-side passivated slice only become significant for depths > 1 mm. However, due to the very low charge carrier density towards the rear side accompanied by a very low detector sensitivity for PL emission at such depth, these differences render negligible for the intensity-weighted mean, which is identical for both cases in our example ($\Delta n_{\text{iwm}} = 1.8 \cdot 10^{14}$ cm^{-3}).

Figure 2 shows the interstitial iron concentration measured at a vertical slice of half a G1-sized mc-silicon ingot. The two insets show 2-D simulations of the dissolved iron concentration with Sentaurus Process [23] taking the precipitation at crystal defects during the crystallization process into account. The Fe distributions are taken from our experimentally verified simulations of the Fe contamination during the crystallization process [24]. These simulations are performed independently of the measurements, as explained in detail in [24, 25].

Both the absolute values of measured and simulated [Fe$_i$] as well as the width of the edge-region affected by solid-state diffusion of iron from the crucible into the crystal during ingot cooling are in excellent agreement. Local differences related to the crystal structure are observed at certain grain boundaries and dislocation clusters, which can be explained by the constant dislocation density of $8 \cdot 10^3$ cm^{-2} used for the simulations [24-26]. This is a realistic dislocation density in grains of mc silicon [26]. However, in areas of dislocation clusters, the actual dislocation density is significantly larger. This effect is not taken into account in the simulations. Slight differences in the width of the edge region between measurement and simulation in the upper part can be attributed to deviations of the real temperature profile in the rectangular crucible from the radially symmetrical temperature profile used as input for the simulations. Additionally, the width of the real crucible slightly widens towards the top, whereas the simulations are based on vertical crucible walls.
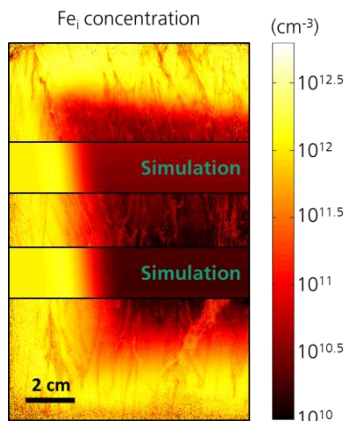
Figure 2: Interstitial iron concentration measured at a vertical slice of half a G1-sized mc-Si ingot in comparison with 2-D simulations of [Fe$_i$]. Large concentrations of interstitial iron stemming from solid-state diffusion into the crystal during ingot cooling are found in the regions close to the crucible walls (left and bottom), whereas large concentrations in the top region are attributed to back-diffusion of segregated iron from the ingot top.

3.2 Measuring bulk lifetime and interstitial iron concentration at unpassivated silicon ingots

Preparation of vertical silicon slices can be avoided completely, if bulk lifetime and interstitial iron concentration can be measured at unpassivated silicon ingots. Lacking surface passivation, polished silicon ingot side facets feature surface recombination velocities in the range of about $2 \cdot 10^5$ cm·s^{-1} [2]. Bulk lifetime contrast of excess carrier density and thus PL intensity is therefore largely disguised by surface recombination. This renders steady-state bulk carrier lifetime approaches much prone to systematic error due to e.g. lateral optical blurring [27], lateral surface morphology variations, an uncertainty of temperature-dependent band-to-band optical absorption properties, or variations and uncertainty of the minority carrier diffusion coefficient.

Dynamic decay time techniques such as harmonically modulated luminescence overcome such limitation, because they allow us to directly investigate the decay time of surviving excess carriers within the bulk rather than to implicitly infer lifetimes from cumulative excess carrier density vastly dominated by surface recombination. Equipped with a detailed understanding of harmonically modulated lifetime [28, 29], we are able to precisely and accurately determine bulk lifetime from such harmonically modulated decay time measurement design.

Figure 3 illustrates such capability via the most extreme case of a virtually undoped and unpassivated float zone silicon ingot. While measurement raw data would not even allow recognizing any harmonic modulation in the PL signal (mostly due to thermal noise originating from the photodetector), the depicted spectrally filtered signal allows determination of a harmonically modulated lifetime of 243 ± 11 µs (790 nm irradiation wavelength),

which corresponds to a bulk lifetime of 612 ± 30 µs. Cumulative excess carrier density (proportional to PL intensity here) would only vary by ± 2 % within this uncertainty range, which would render steady-state approaches highly susceptible to systematic error even in view of minor perturbations.

Notably, the high bulk lifetime contrast of harmonically modulated luminescence on unpassivated ingots opens novel pathways in material investigations involving highest bulk lifetimes beyond the performance limit of state-of-the-art wafer surface passivation techniques. Rather than taking the risk of possibly insufficient surface passivation disguising bulk lifetime information, a more accurate alternative would be to investigate unpassivated bulk samples.
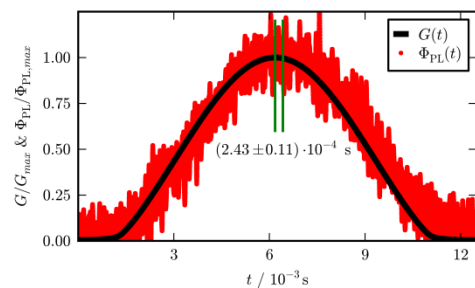

Figure 3: Extreme case of a harmonically modulated PL lifetime measurement (G: excess carrier generation rate, Φ_{PL}: PL intensity) on a virtually undoped float zone silicon ingot without surface passivation. Even here, bulk lifetime can be inferred from the harmonically modulated lifetime at an astonishing precision.

It should also be noted that the harmonically modulated approach proved eligible for accurate bulk lifetime calibration of steady-state PL images [8] – as particularly detailed for unpassivated ingots in [15], and as used in the following. Figure 4 exemplarily shows a calibrated lifetime image at low injection level of the lower left corner of an unpassivated high-performance mc-Si ingot in the Fe$_i$-state after splitting of FeB-pairs. Together with a lifetime image in the FeB-state, this is used as input for imaging the concentration of interstitial iron at unpassivated silicon ingots, as explained in the following.
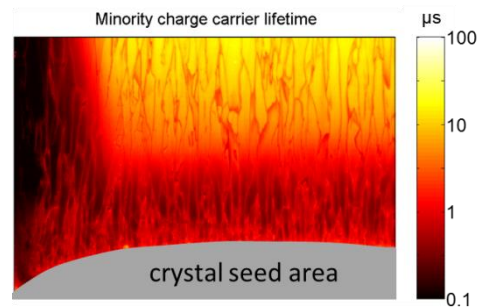

Figure 4: Calibrated bulk-lifetime image of the lower left corner of an unpassivated high-performance mc-Si ingot side facet according to a harmonically modulated calibration approach detailed in [15].

Recently, Mitchell *et al.* presented a method for measuring the interstitial iron concentration directly on the

side face of silicon ingots by spectral PL intensity ratio imaging [3]. Here, we present an approach for Fe-Imaging on bare silicon ingots, also based on FeB-pairing and –splitting, in combination with the aforementioned ingot bulk lifetime calibration by modulated PL, featuring an exceptionally high sensitivity. This technique relies on a careful pairing and splitting of FeB-pairs. The largest challenge is to reach sufficiently high injection levels for FeB-splitting, which we achieve by laser-illumination with an irradiation intensity of approximately 20 suns. In order to achieve sufficiently high injection levels, the ingot is illuminated with two lasers of different wavelengths (790 nm and 940 nm). Besides acting as additional illumination source, the 940 nm laser features a larger penetration depth in silicon (~ 55 µm) compared with the 790 nm laser of the measurement setup (~ 11 µm). Due to the lacking front-surface passivation, the deeper penetration depth significantly increases the excess charge carrier density, which is shown in Figure 5: $\Delta n(z)$ is increased by a factor of ~ 5 for illumination with the 940 nm laser (red dashed line compared with orange dashed line). While at standard measurement conditions of 1 sun illumination the charge carrier density is below 10^{13} cm^{-3} for a bulk lifetime of 100 µs, injection levels sufficiently high for FeB-splitting are achieved by an illumination with ~ 20 suns in combination with the deeper penetration depth of the 940 nm laser.
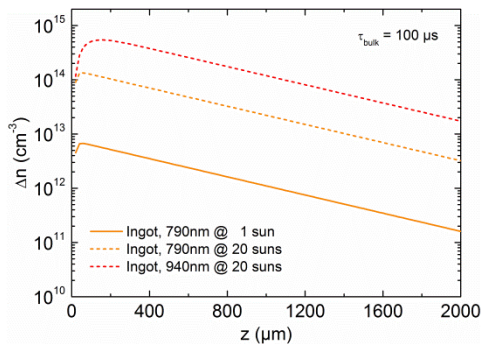
Figure 5: Comparison of excess charge carrier profiles in the first 2 mm of an unpassivated silicon ingot at measurement conditions of 1 sun and at FeB-splitting conditions at 20 suns for illumination with the 790 nm or 940 nm laser (constant bulk lifetime 100 µs).
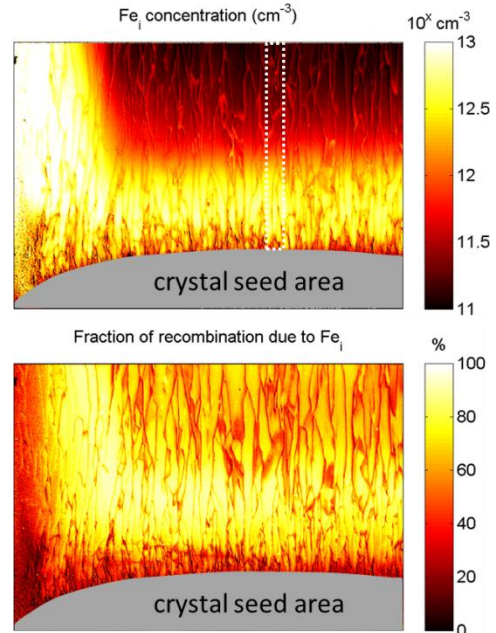
Figure 6 shows images of the interstitial iron concentration and the fraction of recombination due to Fe$_i$ measured on the side face of an unpassivated multicrystalline silicon ingot by this method. In order to validate the measurements, we performed independent 2-D simulations with Sentaurus Process as in the previous section. In the simulations, the Fe diffusion from the crucible walls into the solid and liquid silicon, segregation during crystallization and back-diffusion is modeled as for standard mc silicon ingots [3, 24] using the measured Fe concentrations in the crucible and coating as input parameters. We estimate that before the melting process around 30% of the seed layer volume is gas-filled voids. As soon as the melting process starts liquid silicon flows

into these voids and re-crystallizes. The re-crystallization is not a continuous process and thus the Fe concentration in the re-crystallized silicon of the seed layer is not reduced by strong segregation from solid to liquid silicon. In consequence the seed layer has a quite high Fe concentration (~3×10^{14} cm^{-3}) and acts as a source for Fe diffusion into the liquid and solid silicon above the seed layer.

Figure 6: Image of the interstitial iron concentration and the fraction of recombination due to Fe$_i$, measured on the side face of an unpassivated high-performance mc-Si ingot.

Figure 7 shows an averaged line-scan of the measured interstitial iron concentration as indicated by the white rectangle in the [Fe$_i$]-image of Figure 6, together with two simulations. The red dotted curve is a simulation of the vertical profile of the interstitial iron concentration, showing the region of solid-state in-diffusion of iron from the crucible bottom and the crystal seed area up to an ingot height of ~ 4 cm (distance from seed). Thereafter, the interstitial iron concentration increases again due to segregation of iron dissolved in the silicon melt. In contrast, the measured iron profile (black symbols) shows a continuous decrease with increasing ingot height. This can be attributed to the distance of the side facet where the iron concentration was measured from the crucible wall being smaller (3.3-3.6 cm) than the width of the region additionally affected by solid-state in-diffusion of iron from the facing crucible wall (*cf.* Figure 8), which leads to an additional two-dimensional increase in iron concentration across the whole measured area. Accounting for this effect in the simulations results in the green dashed curve, which is in good agreement with the measured interstitial iron concentration and validates the method. The decrease in the measured values close to the seed can be attributed to an increase in grain boundary and dislocation density (see Figure 4) which is not taken into account in the simulations. Slight deviations between

measurement and simulations for ingot heights larger than 2.5 cm can be related to the uncertainty of the distance of the side facet from the crucible wall, leading to an uncertainty in the simulated interstitial iron concentration.
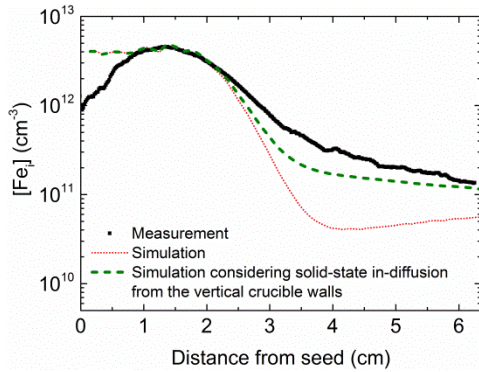

Figure 7: Measured and simulated interstitial iron profiles close to the seed area of a high-performance multicrystalline silicon ingot.
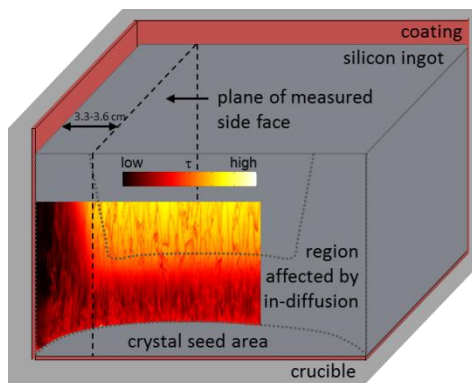

Figure 8: Illustration of the plane of the measured side face with a distance of 3.3-3.6 cm from the crucible wall. In the lower part of the ingot, this plane is significantly affected by solid-state in-diffusion of iron from the facing crucible wall as indicated by the dotted line, resulting in the shift from the red dotted to the green dashed Fe_i-profile in Figure 7

3.3 Specification of bulk-related efficiency loss mechanisms

An "Efficiency Limiting Bulk Recombination Analysis" (ELBA) [16, 17] combines injection-dependent charge carrier lifetime images obtained from calibrated PLI of wafers processed according to a certain cell process with PC1D solar cell simulations of a specific solar cell concept and, thus, allows for a prediction of the material-related efficiency potential for the cell concept under investigation. Further, it enables a quantification of the specific loss mechanisms in the bulk [30, 31], separating between losses due to homogeneously distributed recombination centers, structural crystal defects and impurities in the edge region. In this paper, we present an advanced procedure of this loss analysis which enables an in-depth understanding of the physical origins for materi-

al-related efficiency losses by separating between recombination- and diffusion-related losses.

In a homogeneously illuminated silicon wafer or solar cell, minority charge carriers diffuse from areas of low recombination to such of high recombination, which leads to a charge carrier redistribution and, thus, a smearing of PL images. On the one hand, lateral carrier diffusion is a physical effect also occurring in a solar cell under working condition and, therefore, needs to be accounted for in a correct prediction of solar cell efficiencies. On the other hand, it conceals the real recombination properties of the material and impedes an exact identification of the specific loss mechanisms. The approach presented here combines an ELBA analysis based on images of the effective charge carrier lifetime comprising lateral carrier diffusion with an ELBA analysis based on de-smeared images of the real charge carrier lifetime. The de-smeared lifetime images are calculated from the effective lifetime images using the continuity equation, as explained in [32].

In order to highlight the effect of lateral carrier diffusion, Figure 9 shows a calibrated PL-image [8] of the effective minority charge carrier lifetime (comprising lateral carrier diffusion) of an n-type high-performance multicrystalline silicon wafer after boron and phosphorus diffusion at an illumination of 0.03 suns (upper image), which suggests that the material features grains of varying material quality.
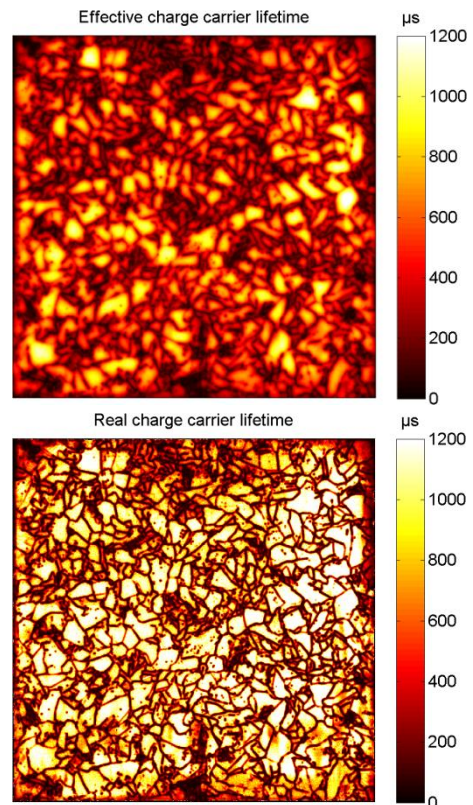

Figure 9: Minority charge carrier lifetime in a processed (B- and P-diffusion) n-type high-performance multicrystalline silicon wafer including lateral charge carrier diffusion (top) or not (bottom) at an illumination of 0.03 suns.

A calculation of the real local minority charge carrier lifetime (Figure 9, lower image) reveals that the inner-grain lifetime is virtually constant across the whole wafer. Thus, differences in the effective lifetime between different grains can be attributed to lateral charge carrier diffusion. Additionally, the de-smeared image shows that the main challenge for optimizing high-performance multicrystalline silicon is to reduce recombination active structural crystal defects, which not only lead to decreased charge carrier lifetimes at the structural defects themselves, but also significantly reduce the charge carrier lifetime in good grains due to lateral carrier diffusion.

For a quantification of loss mechanisms, effective efficiency maps (η_{eff}) are obtained from a first ELBA analysis based on injection-dependent effective lifetime images. The global efficiency potential for the entire wafer compared with the efficiency limit of the solar cell without recombination losses gives access to the total material-related losses, comprising recombination losses and diffusion losses in grains as well as recombination losses at structural crystal defects. Together with de-smeared efficiency maps ($\eta_{de\text{-}smeared}$) obtained from a second ELBA analysis based on injection-dependent de-smeared lifetime images, a separation of these loss mechanisms becomes possible: Relating the efficiency potential in the grains obtained from $\eta_{de\text{-}smeared}$ to the cell limit quantifies the recombination losses in the grains, whereas the efficiency potential in the grains obtained from η_{eff} additionally includes the losses due to lateral charge carrier diffusion to recombination active structural crystal defects. Finally, the difference between the total losses obtained from η_{eff} and the recombination and diffusion losses in the grains assesses the losses due to recombination at structural crystal defects. Figure 10 shows such a loss analysis on the example of n-type high-performance multicrystalline silicon after a solar cell process including a boron diffusion or a boron and a phosphorus diffusion for a high-efficiency solar cell concept featuring a cell limit of 23.1%. The advanced analysis based on de-smeared lifetime images reveals that approximately one third of the inner grain losses are actually due to lateral charge carrier diffusion to recombination active structural crystal defects. Note that this value depends on the size of the chosen grain as well as the chosen border between grain and surrounding grain boundaries. Nevertheless, this would only alter the ratio of structural crystal defect-related losses attributed to diffusion losses or recombination losses (shift the margin between the hatched and the double-hatched gray parts of the columns as indicated by the arrows in Figure 10), while the total structural crystal defect-related losses and the recombination losses in grains remain unaffected by the choice of the specific grain and border. Being responsible for diffusion losses in grains and direct recombination losses at grain boundaries, structural crystal defects account for the major part of efficiency losses in n-type high-performance multicrystalline silicon. This highlights the importance of reducing the recombination activity of grain boundaries

in high-performance mc-Si. One possibility is the application of a phosphorus gettering diffusion, which approximately cuts in half the recombination losses at grain boundaries (c.f. Figure 10). Improving the crystallization process or applying a hydrogenation step would be further steps to close the gap between efficiencies of multi- and monocrystalline silicon solar cells.
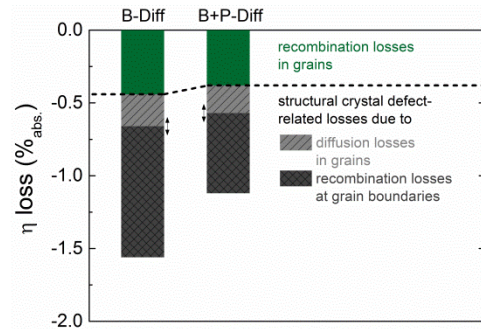

Figure 10: Advanced quantification of loss mechanisms in n-type high-performance multicrystalline silicon.

4 CONCLUSION

This contribution elaborates on progress with the investigation of silicon material limits via state-of-the-art photoluminescence techniques. The very high bulk lifetime sensitivity of harmonically modulated luminescence allows most accurate investigation of highest quality bulk samples and detailed material studies such as metastable defect imaging on the level of unpassivated ingots. Separating effects of lateral carrier diffusion in ELBA gives rise to a refined assessment of multicrystalline performance limits due to structural crystal defects.

5 ACKNOWLEDGEMENT

REFERENCES

[1]   B. Michl, M. Padilla, I. Geisemeyer, S. T. Haag, F. Schindler, M. C. Schubert, and W. Warta, IEEE Journal of Photovoltaics **4** (2014) 1502.

[2]   J. A. Giesecke, R. A. Sinton, M. C. Schubert, S. Riepe, and W. Warta, IEEE Journal ofPhotovoltaics **3** (2013) 1311.

[3]   B. Mitchell, D. Macdonald, J. Schon, J. W. Weber, H. Wagner, and T. Trupke, IEEE Journal of Photovoltaics **4** (2014) 1185.

[4]   J. Haunschild, I. E. Reis, T. Chipei, M. Demant, B. Thaidigsmann, M. Linse, and S. Rein, Solar Energy Materials & Solar Cells **106** (2012) 71.

[5]   S. Y. Lim, M. Forster, X. Zhang, J. Holtkamp, M. C. Schubert, A. Cuevas, and D. Macdonald, IEEE Journal of Photovoltaics **3** (2013) 649.

[6]   T. Trupke, R. A. Bardos, M. C. Schubert, and W. Warta, Applied Physics Letters **89** (2006) 1.

[7]   T. Trupke, R. A. Bardos, and M. D. Abbott, Applied Physics Letters **87** (2005) 184102.

[8]   J. A. Giesecke, M. C. Schubert, B. Michl, F. Schindler, and W. Warta, Solar Energy Materials and Solar Cells **95** (2011) 1011.

[9]   M. C. Schubert, H. Habenicht, and W. Warta, IEEE Journal of Photovoltaics **1** (2011) 168.

[10]   D. Macdonald, J. Tan, and T. Trupke, Journal of Applied Physics **103** (2008) 073710.

[11]   H. Habenicht, M. C. Schubert, and W. Warta, Journal of Applied Physics **108** (2010) 034909.

[12]   S. Y. Lim, F. E. Rougieux, and D. Macdonald, Applied Physics Letters **103** (2013) 092105.

[13]   T. Niewelt, S. Lim, J. Holtkamp, J. Schön, W. Warta, D. Macdonald, and M. C. Schubert, Solar Energy Materials and Solar Cells **131** (2014) 117.

[14]   L. E. Mundt, M. C. Schubert, J. Schön, B. Michl, T. Niewelt, F. Schindler, and W. Warta, IEEE Journal of Photovoltaics **5** (2015) 1503.

[15]   J. A. Giesecke, M. C. Schubert, F. Schindler, and W. Warta, IEEE Journal of Photovoltaics **5** (2015) 313.

[16]   B. Michl, M. Rüdiger, J. Giesecke, M. Hermle, W. Warta, and M. C. Schubert, Solar Energy Materials & Solar Cells **98** (2012) 441.

[17]   B. Michl, M. Kasemann, W. Warta, and M. C. Schubert, Physica Status Solidi RRL – Rapid Research Letters **7** (2013) 955.

[18]   M. C. Schubert, H. Habenicht, M. J. Kerler, and W. Warta, Solid State Phenomena **156-8** (2010) 407.

[19]   J. Giesecke, *Quantitative Recombination and Transport Properties in Silicon from Dynamic Luminescence*. (Springer, 2014).

[20]   S. Bowden and R. Sinton, Journal of Applied Physics **102** (2007) 124501.

[21]   S. Herlufsen, D. Hinken, M. Offer, J. Schmidt, and K. Bothe, IEEE Journal of Photovoltaics **3** (2013) 381.

[22]   F. D. Heinz, J. Giesecke, L. E. Mundt, M. Kasemann, W. Warta, and M. C. Schubert, Journal of Applied Physics **118** (2015) 105706.

[23]   Synopsys, (2012).

[24]   M. C. Schubert, J. Schön, F. Schindler, W. Kwapil, A. Abdollahinia, B. Michl, S. Riepe, C. Schmid, M. Schumann, S. Meyer, and W. Warta, IEEE Journal of Photovoltaics **3** (2013) 1250.

[25]   F. Schindler, B. Michl, J. Schön, W. Kwapil, W. Warta, and M. C. Schubert, IEEE Journal of Photovoltaics **4** (2014) 122.

[26]   J. Schön, H. Habenicht, M. C. Schubert, and W. Warta, Journal of Applied Physics **109** (2011) 1.

[27]   D. Walter, A. Liu, E. Franklin, D. Macdonald, B. Mitchell, and T. Trupke, in Proceedings of the 38th IEEE Photovoltaic Specialists Conference, Austin, USA (2012) 307.

[28]   J. A. Giesecke and W. Warta, Applied Physics Letters **104** (2014) 082103.

[29]   J. A. Giesecke, S. W. Glunz, and W. Warta, Journal of Applied Physics **113** (2013) 073706.

[30]   F. Schindler, B. Michl, A. Kleiber, H. Steinkemper, J. Schon, W. Kwapil, P. Krenckel, S. Riepe, W. Warta, and M. C. Schubert, IEEE Journal of Photovoltaics **5** (2015) 499.

[31]   F. Schindler, *Electrical Material Properties and Efficiency Limits of Compensated and Multicrystalline Silicon for Solar Cells*, PhD thesis, Albert-Ludwigs-Universität Freiburg im Breisgau (2015).

[32]   S. P. Phang, H. C. Sio, and D. Macdonald, Applied Physics Letters **103** (2013) 192112.